

Bulk modulus of H₂O across the ice VII–ice X transition measured by time-resolved x-ray diffraction in dynamic diamond anvil cell experiments

A. S. J. Méndez ^{1,2,*}, F. Trybel ², R. J. Husband ¹, G. Steinle-Neumann ², H.-P. Liermann ¹ and H. Marquardt ³

¹Deutsches Elektronen-Synchrotron (DESY), 22607 Hamburg, Germany

²Bayerisches Geoinstitut, Universität Bayreuth, 95440 Bayreuth, Germany

³Department of Earth Sciences, University of Oxford, OX1 3AN Oxford, United Kingdom



(Received 25 June 2020; revised 19 October 2020; accepted 4 January 2021; published 17 February 2021)

We have studied the H₂O ice VII–ice X phase transition at room temperature by performing three quasi-continuous synchrotron time-resolved x-ray-diffraction experiments in a dynamic diamond anvil cell, reaching pressures of 180 GPa. The dense pressure coverage of our volume data allows us to directly derive the bulk modulus for H₂O over the entire pressure range. Our data document three major changes in compression behavior in the ranges of 35–40, 50–55, and 90–110 GPa, likely corresponding to the formation of pretransition dynamically disordered ice VII and ice X, and static ice X, respectively. Our results confirm that ice X has a very high bulk modulus.

DOI: [10.1103/PhysRevB.103.064104](https://doi.org/10.1103/PhysRevB.103.064104)

I. INTRODUCTION

H₂O ice is present in a large variety of planetary bodies, including the ice giants, Uranus and Neptune, mini-Neptune exoplanets [1,2], and icy satellites [3,4], having a fundamental impact on the heat and chemical exchange in their interiors [5–8]. H₂O ice might also be present in Earth’s deep mantle, as well as other terrestrial planets, where it can form through mineral dehydration reactions occurring at relatively cold regions of the mantle [9–11]. The polymorphs ice VII and ice X are the stable forms of H₂O ice that exist at pressures (P) larger than 2 GPa, and their physical properties play a pivotal role in the structure and evolution of H₂O-rich planetary bodies.

Ice VII is a solid characterized by a body-centered-cubic (bcc) arrangement of oxygens, with H₂O molecules linked via hydrogen bonds (O–H···O) such that the ice rules are satisfied [12]. The high- P phase ice X is based on the same bcc oxygen lattice, but hydrogen atoms are located symmetrically between two oxygen atoms (O–H–O). It has been proposed that the ice VII–ice X transition proceeds through a proton order-disorder transition in which H₂O molecules dissociate, triggered by changes in the energy potential for the O–H···O bond with P , leading to the formation of pretransitional states prior to complete bond symmetrization in ice X [13–16]. At low P , the energy potential determining the position of the protons has been predicted to be of double-well character with a high-energy barrier and a localized proton position coinciding with one of the two minima [17]. Computational studies [13–17] describe three main changes in the energy potential of the H bond across the ice VII–ice X transition: (i) A lowering of the energy barrier with P triggers proton tunneling between the two minima, forming the translationally or dynamically disordered ice VII (ice VII′). (ii) As the potential barrier

approaches zero with P , the proton distribution shifts to the center, forming the dynamically disordered ice X (ice X′). (iii) Symmetrization is complete when the energy potential adopts a narrow single-well form, localized at the midpoint between two oxygens (O–H–O), forming the static ice X.

Numerous experimental studies employing different techniques, including x-ray diffraction (XRD) [18,19] and neutron diffraction [20], Raman [21], and infrared (IR) spectroscopy [22–25], as well as refractive index measurements [26], reported anomalies between 40 and 75 GPa, possibly associated with the formation of the dynamically disordered states. Diffraction [18,20,27] and IR measurements [23,25] have reported O–H–O bond symmetrization in the P range of 110–140 GPa, while Raman [28] and optical measurements [26] suggest an onset at $P \approx 90$ GPa. However, these experimental techniques do not probe proton dynamics directly, and the formation of the pretransitional states cannot be detected unambiguously. Recently, Meier *et al.* [29] reported first direct observations of proton mobility for $P = 8$ –90 GPa by a line-shape analysis of nuclear magnetic resonance (NMR) experiments.

Here we perform compression experiments in combination with time-resolved XRD in order to explore the compressive behavior of H₂O across the ice VII–ice X transition up to 180 GPa using a dynamic diamond anvil cell (dDAC) driven by a piezoelectric actuator [30,31]. This setup provides quasicontinuous volume- P data, with hundreds of diffraction patterns recorded in one experiment, and therefore allows us to compute compressibility by numerical differentiation without invoking an equation of state model to fit the data [32], a significant advance over prior static experiments with tens of data points. We track the bulk modulus evolution across the ice VII–ice X transition, and explore whether this transition as well as the pretransitional states (ice VII′ and ice X′) can be detected from changes in the compression behavior.

*alba.mendez@desy.de

TABLE I. Summary of experimental run conditions.

Run No.	Culet size (μm)	Gasket type	Sample-detector distance (mm)	Maximum pressure (GPa)	Experiment total time (s)	Nominal compression rate (GPa/s)	Exposure time (ms)	Number of images analyzed
dDAC-1	150	Amorphous	418.42	90	300	0.5	100	1800
dDAC-2	100	Re	166.31	160	850	0.4	1000	590
dDAC-3	80	Re	404.89	180	868	0.6	2000	305

II. METHODS

A. Experimental setup

Three symmetric piston cylinder-type DACs are equipped with 150-, 100-, and 80- μm -diameter culet anvils (dDAC-1, dDAC-2, and dDAC-3), with two different gasket configurations (Table I): (i) In dDAC-2 and dDAC-3, regular Re gaskets are preindented to a thickness of 30 μm and holes of 50- and 40- μm diameters are drilled, respectively; (ii) In dDAC-1, an amorphous gasket is employed in order to avoid the emergence of diffraction peaks from the Re gasket. A disk of an amorphous boron alloy ($\text{Fe}_{0.79}\text{Si}_{0.06}\text{B}_{0.15}$) with a thickness of 30 μm and a 50- μm -diameter hole is inserted in a Re gasket, preindented to the same thickness, following the procedure described in Méndez *et al.* [33].

Milli-Q H_2O is loaded along with Au powder (99.99% pure from Sigma-Aldrich) as P marker and a ruby chip to monitor P in the sample during precompression. DACs are inserted in a “cap housing” coupled to a high-voltage piezoelectric actuator (PEA) as described in Jenei *et al.* [31]. DAC and PEA are coupled by tightening the end cap at the back of the housing until a P increase of 1–2 GPa is observed. The PEA is connected to an amplifier (Piezosystem Jena GmbH), remotely controlled via a waveform generator (Agilent 33522B). When voltage is applied, the PEA in contact with the DAC continuously expands, pushing directly onto the piston in a controlled and smooth manner, avoiding abrupt pressure changes in the sample. Trapezoidal voltage-time waveforms are created by the Agilent BENCHLINK waveform builder software by Keysight and sent to the PEA. We chose voltage-time waveforms to achieve nominal compression rates of 0.4–0.6 GPa/s that permits for sufficiently long x-ray exposure times while still achieving an excellent resolution in P sampling (Table I).

B. X-ray diffraction

Monochromatic synchrotron x-rays with a fixed wavelength (0.4828 Å) are used for time-resolved diffraction experiments at the Extreme Conditions Beamline P02.2 at PETRA III, Hamburg, Germany [34]. A compound refractive-lens focused x-ray beam [3 μm (h) \times 8 μm (v) full width at half maximum] is aligned with the center of the sample chamber. GaAs 2.3 MPix LAMBDA detectors, with a pixel size of 55 $\mu\text{m} \times 55 \mu\text{m}$ and a repetition rate of up to 2 kHz, are employed to perform fast collection of XRD images [35,36]. For dDAC-2, one detector is aligned with the sample center and placed at a short sample to detector distance (Table I), ensuring the collection of full diffraction rings. For dDAC-1 and dDAC-3, two detectors are symmetrically offset from the direct beam, capturing sections of the Debye-Scherrer

diffraction rings. Tilting of the detector(s) and the sample-detector distance are calibrated using a Cr_2O_3 standard (NIST 674b). With this setup we collect 305–1800 individual x-ray-diffraction patterns in each compression experiment (Table I). In-house data analysis software is used for quick visualization of the collected data (Fig. 1).

C. Diffraction pattern fitting

The detector images are radially integrated using the DIOP-TAS software [37] to obtain 1D diffraction patterns as a function of the 2θ angle (Fig. 2). During integration, the dead areas of the detectors are masked to improve the signal/noise ratio. Additionally, the most intense areas of the (101) diffraction ring of Re–(101)_{Re} are masked in dDAC-2 in order to minimize the convolution with the (110)_{iceVII} diffraction ring (Fig. 3).

A PYTHON routine is developed to deal with the large number of diffraction patterns (Table I) and to automate peak fitting and tracking. Before integrated patterns are processed by the routine, we average over three points in 2θ space and apply an infinite impulse response (IIR) filter forwards and backwards with zero phase shift to further improve the signal/noise ratio and the reliability as well as the speed of the

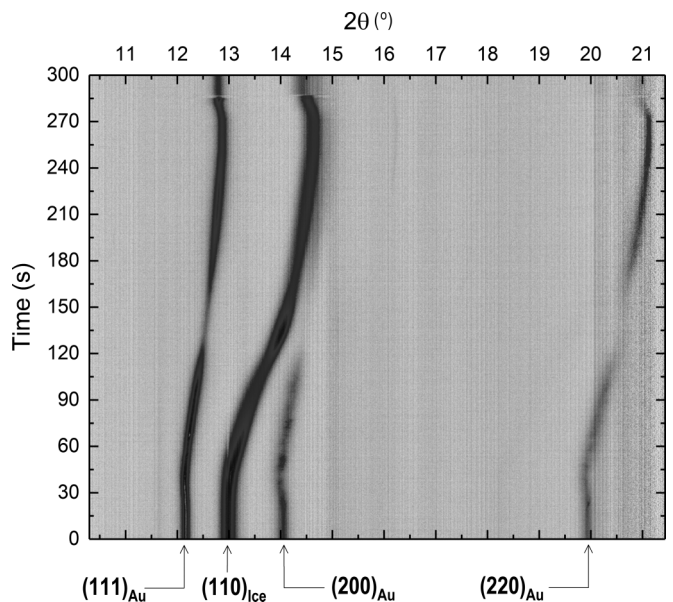


FIG. 1. Contour plot showing the time evolution of diffraction patterns (peaks) collected for dDAC-1 in time- 2θ space. In our experiments, the (110) diffraction line of ice VII is the most intense and can be traced over the full P range of the individual experiments.

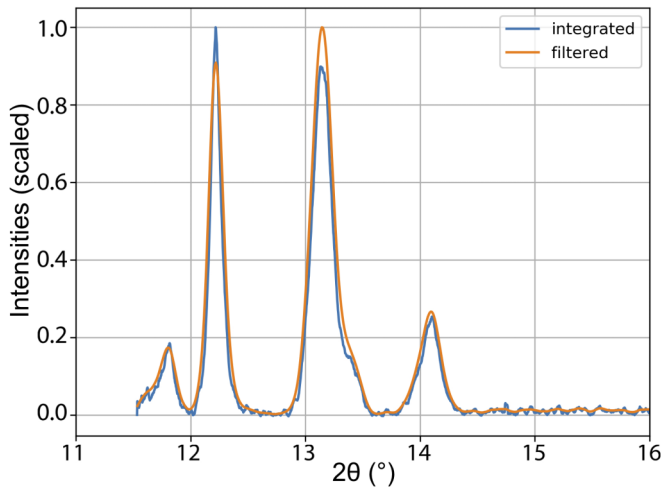


FIG. 2. Exemplary integrated diffraction pattern for the dDAC-2 experiment at 26 GPa. Blue shows the original pattern after integration of the detector image with DIOPTAS; orange the pattern after application of an IIR filter with zero phase shift.

fitting routine (Fig. 2). In order to analyze the recorded diffraction data, the peaks in the window $2\theta = 11.0^\circ\text{--}20.0^\circ$ are assigned to a crystal structure, fitted and positions are tracked over the entire compression range in all diffraction patterns. In a first step, the positions of the expected peaks (indices identified via peak comparison with DIOPTAS) are calculated from the space group and a given initial compression using a routine from the *pymatgen* (Python Materials Genomics) library [38]. The calculated peak positions (CPPs) are used as the initial positions for a model consisting of a Gaussian for each peak and a linear background correction. The model is optimized with a nonlinear least-squares fit to obtain optimal peak positions (OPP) employing the LMFIT package [39]. The OPP of the individual Gaussians are subsequently compared with the prediction (CPP); if an individual OPP is at larger (smaller) 2θ angle than CPP, compression is increased (decreased) until $|\text{OPP} - \text{CPP}| < \epsilon$ is reached (with ϵ a convergence parameter). The optimization of the compression is performed with an adaptive step width to improve accuracy and runtime.

As the P standard and the sample differ in compressional behavior, the peak positions are optimized separately: P is calculated using the optimized position of $(111)_{\text{Au}}$ combined with the equation of state of Fei *et al.* [40]. Volume (V) of H₂O ice is determined from $(110)_{\text{iceVII}}$. The $(200)_{\text{Au}}$ peak of the P standard and $(101)_{\text{Re}}$ from the gasket (dDAC-2 and dDAC-3) are included to improve the model, but not considered in the optimization. In particular, $(200)_{\text{Au}}$ is not suitable for that purpose as it is small in amplitude and the amplitude decreases with P .

Diffraction patterns are individually loaded with user input on the initial compression estimate. Although the program can handle each spectrum individually, it is significantly more efficient to guess a starting compression from the previous P step. This especially helps to resolve overlapping peaks, where a good initial guess is crucial. Such an interaction between $(110)_{\text{iceVII}}$ and $(101)_{\text{Re}}$ is shown in Fig. 3. At low P , $(110)_{\text{iceVII}}$ appears at a smaller 2θ -value than $(101)_{\text{Re}}$; during

compression, the peaks start to overlap at $P > 20$ GPa and reverse order in 2θ at $P > 40$ GPa.

The routine can resolve the individual peaks when they are partly overlapping by estimating a linear compression rate. However, if the peaks are completely overlapping, a reliable fit is not possible, and, for this reason, for dDAC-3 a small P range (41–49 GPa) is not processed. Nevertheless, we obtain, especially for dDAC-2 with a full diffraction ring, dense $V(P)$ data with only very small data scatter introduced by the fitting routine due to peak asymmetry and overlap. The error in V is calculated from the minimal separable peak distance in the routine (0.05° in 2θ). If the peak shift between two consecutive patterns is too small, the program tends to keep the positions constant, followed by a sudden jump to another configuration. In principle, this problem can be avoided by decreasing ϵ from 10^{-3} to 10^{-5} for $|\text{OPP} - \text{CPP}|$ determination. However, prohibitively increased computational requirements make fitting all patterns with $\epsilon = 10^{-5}$ impossible. Instead, we use every 25th diffraction pattern for dDAC-1, every 10th for dDAC-2, and every 5th for dDAC-3, preserving an excellent P resolution, i.e., 1 GPa for dDAC-1 and 3 GPa for dDAC-2 and dDAC-3 (for an extended discussion see the Supplemental Material [41]).

Fitting a series of Gaussians rather than performing a Rietveld or Le Bail refinement has large advantages for the current datasets: The standard refinement techniques rely on the peak shape which may cause problems for the peak overlap discussed above, and processing the data is even more challenging in terms of automation. Nevertheless, on a limited number of diffraction patterns from dDAC-1 and dDAC-2 we have tested that P and V obtained from the Gaussian fitting performed here and a Le Bail refinement. The results are consistent with one another within the error coming from the minimal separable peak distance in our approach (Table I in the Supplemental Material [41]).

D. Bulk modulus calculation

The isothermal bulk modulus (K_T) can be directly calculated from our dense $V(P)$ dataset via $K_T = -V \cdot \partial P / \partial V$, with the advantage that no assumption has to be made with respect to the analytical form of an equation of state. Previous DAC studies on ice VII and ice X [18,19,27], by contrast, had to rely on an equation of state fit due to the significantly lower number of data points. Here, using the increased P spacing by not fitting all diffraction patterns as discussed above, becomes a further advantage, as a small denominator (ΔV) can lead to significant fluctuations in the calculated bulk modulus. We further apply a spline interpolation with smoothing [42,43] before calculating the bulk modulus via a central difference scheme to mediate still existing unphysical fluctuations (Fig. S1 in the Supplemental Material [41]). The smoothing factors are chosen such that smooth variations of K_T with P are obtained, while simultaneously keeping the difference between data points and the spline $< 1\%$ over the complete compression range for all experiments [Fig. 4(b)].

The error in K_T is propagated from the error in V with a central difference scheme. As the $(111)_{\text{Au}}$ reflection (P marker) does not suffer asymmetry or overlap, P is assumed to be error-free.

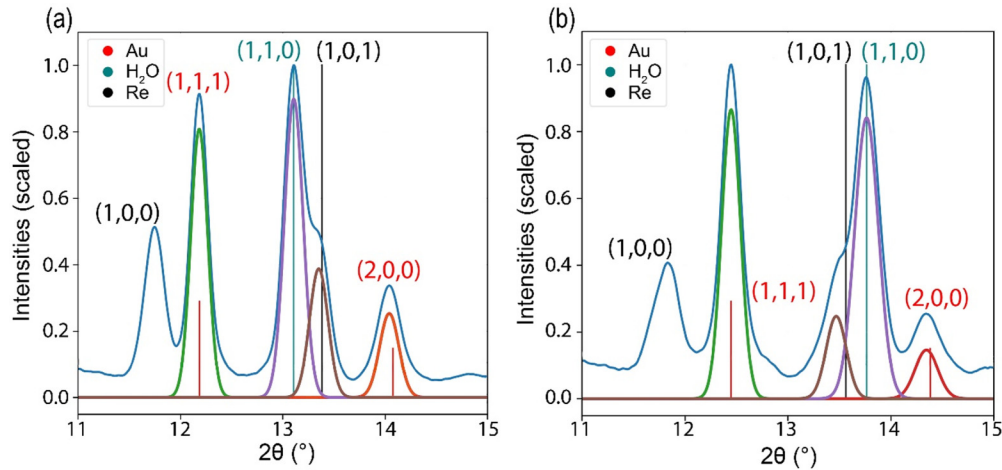


FIG. 3. Diffraction patterns collected from dDAC-3 after application of the IRR filter (blue) at (a) 24 GPa and (b) 45 GPa with assigned indices and the calculated/theoretical peak positions (CPPs) shown as vertical lines. The solid curves represent the Gaussian model peaks.

III. RESULTS AND DISCUSSION

A. Volume compression curve of H₂O ice

Figure 4 shows the unit cell V of H₂O ice as a function of P from our experiments in comparison with previous XRD measurements [18,19,27] and equation of state predictions [44,45]. Differences between V measured in our three runs fall within the refinement uncertainties determined by the resolution limit of 0.05° in 2θ for the diffraction patterns [Fig. 4(a)], suggesting that the choice of the gasket material or the sample-detector configuration do not affect the results significantly. Overall, our $V(P)$ data are in good agreement with previous experimental results [18,19,27] [Fig. 4(c)], and the observed differences in V between our three compression runs (dDAC-1, dDAC-2, and dDAC-3) are similar to differences between previously published measurements [18,19,27], and between the three single-crystal x-ray-diffraction experiments

reported in Loubeyre *et al.* [27]. The scatter that we see in our data within one run is significantly smaller than in any of the experiments previously reported [18,19,27].

Our data generally agree with equations of state based on both experimental data [45] and computational results [44], even though some small but systematic deviations in P trends exist in the P range 50–100 GPa [Fig. 4(c)]. This range coincides with the formation of the disordered ice state(s), likely triggered by nuclear quantum effects occurring in the range $50 \lesssim P \lesssim 70$ GPa [13,14]. French and Redmer [44] computed an analytical thermodynamic potential from *ab initio* calculations based on classical proton trajectories; although their calculations were supplemented with a quantum correction, they did not include tunneling effects, which affect the proton motion and can explain the deviation from our results. The equation of state by Klotz *et al.* [45] is based on the extrapolation of neutron diffraction data measured up to 14 GPa,

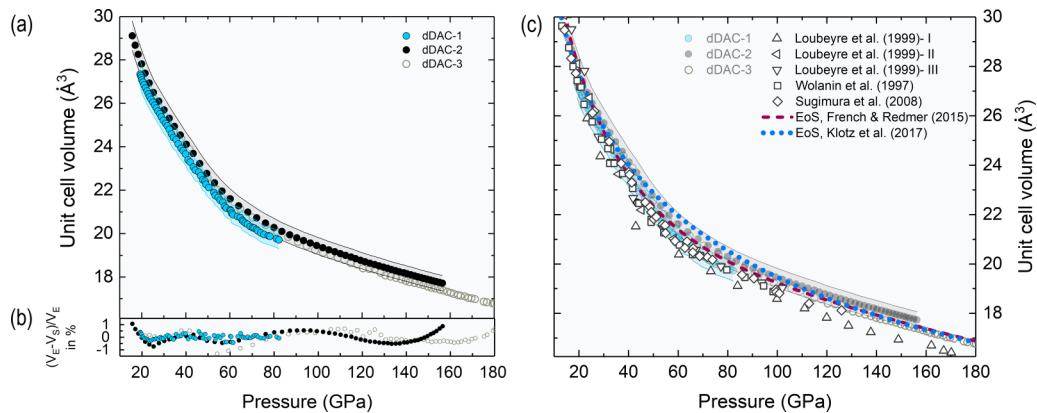


FIG. 4. (a) Volume-pressure points for H₂O ice as derived from the reduced datasets of the dDAC-1 (blue solid circles), dDAC-2 (black solid circles), and dDAC-3 experiments (gray open circles). Error bands using the resolution limit (0.05° in 2θ) of the fitting routine are shown for dDAC-1 and dDAC-2 (shaded regions). (b) Difference between the data points and the spline with smoothing factors of 9.0 (dDAC-1), 1.0 (dDAC-2), and 18.0 (dDAC-3) is $<1\%$ over the complete compression range for all experiments. (c) Previous XRD measurements in static DAC experiments by Wolanin *et al.* [19] (powder, squares), Sugimura *et al.* [18] (powder, diamonds), and Loubeyre *et al.* [27] (three single-crystal datasets, three differently pointing triangles) are plotted in comparison to our data. The dashed (maroon) and dotted (blue) curves represent the equations of state by French and Redmer [44] and Klotz *et al.* [45], respectively, the latter extrapolated significantly beyond the P range of the experiments (14 GPa).

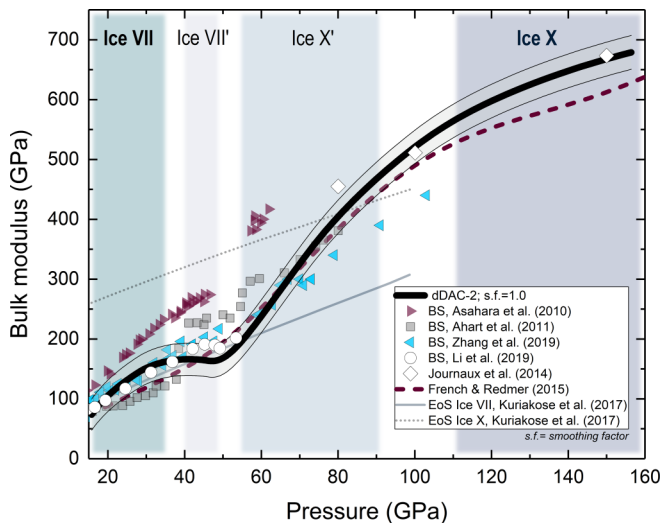


FIG. 5. Bulk modulus of H₂O ice as a function of pressure calculated from the smoothed spline interpolation of the $V(P)$ data from dDAC-2 in comparison to previous studies (for results from dDAC-1 and dDAC-3, see Fig. S2 in the Supplemental Material [41]). Right-pointing triangles, solid squares, left-pointing triangles, and solid circles represent Brillouin inelastic scattering (BS) data [46–49]. The solid and dotted thin gray lines show equations of state for ice VII and ice X, respectively [50]. Diamonds represent computational predictions of the bulk modulus of ice X [51]. The dashed maroon line refers to computational results [44]. Background colors guide the eyes to the approximate P ranges for the stability of ice VII, ice VII', ice X', and ice X based on the P ranges where a quasilinear P dependence of K_T is observed in our work.

which is a too low P for observing significant proton tunneling effects as indicated by the NMR results [29].

B. Bulk modulus of H₂O ice at high pressures

Bulk moduli computed from our splined data (for clarity we only show K_T - P from dDAC-2 in Fig. 5, with the results for dDAC-1 and dDAC-3 in Fig. S2 of the Supplemental Material [41]) agree well with recent Brillouin spectroscopy measurements at $P \lesssim 35$ GPa [46,47]. At higher P , three major changes in the slope of K_T - P are captured by our experiments (Fig. 5):

(i) A softening starting at $P = 35$ –40 GPa indicates a transition towards a more compressible state (Fig. 5), supporting previous findings [18]. We associate this change with the formation of disordered ice VII'. While Brillouin spectroscopy measurements disagree with one another in terms of absolute values for the bulk modulus, they show [47,48]—or at least hint at [46]—a P range of high compressibility (40–50 GPa), supporting our observation. A possible reason for the disagreement between the various Brillouin spectroscopy studies at all P is the marked elastic anisotropy of ice VII and, as a consequence, the possibility that velocities along certain directions were favored by crystallographic preferred orientation and/or selective elasto-optic coupling between the probing laser and specific phonon propagation direction [52]. In the P range where we observe the softening, signal overlap

with the diamond anvils further complicates a reliable determination of the bulk modulus by Brillouin spectroscopy [46].

(ii) A steep increase in K_T starting at $P = 50$ –55 GPa marks the formation of a less compressible phase, coinciding with the onset of hydrogen symmetrization predicted by computations at $P \approx 50$ GPa [13], and may also be associated with anomalies in the infrared spectra of H₂O ice reported for $P = 55$ –62 GPa [23,53,54]. We attribute this feature to the formation of ice X' [18].

(iii) A distinct change in P dependence of K_T at $P = 90$ –110 GPa, which is in excellent agreement with computational predictions [44,51], but has not been documented by previous experiments on the elastic properties of ice VII [18,24,26–28]. We attribute this change to the formation of static ice X.

These changes in the P behavior of K_T are also visible in the dDAC-1 and dDAC-3 data at comparable onset P (Fig. S2 in the Supplemental Material [41]).

The observed P evolution of K_T across the ice VII–ice X transition in our experiments can be correlated with the variations in proton mobility observed by Meier *et al.* [29] for the O–H···O bond, and be rationalized by the predicted evolution of the energy barrier of a double-well potential [17,55]. Meier *et al.* [29] documented a significant increase in tunneling probability for $P = 20$ –50 GPa, i.e., in the P range where the formation of ice VII' is expected. Our observation of a softening of K_T for ice VII observed for $P = 35$ –40 GPa may be explained by a decrease in the “proton pressure” caused by higher proton mobility [18,55]. The steep increase in K_T that we observe for $P > 50$ GPa (Fig. 5) may reflect the proton centering process, and the formation of ice X'. Full proton localization may cause the change of the P derivative in our K_T data for $P = 90$ –110 GPa.

IV. CONCLUSIONS

We have collected quasicontinuous x-ray-diffraction data across the ice VII–ice X transition and up to $P = 180$ GPa in three dynamically driven diamond anvil cell experiments. We derive the bulk modulus of H₂O ice directly from our $V(P)$ data. We find three main changes in the pressure dependence at 35–40, 50–55, and 90–110 GPa and associate them with the formation of ice VII', ice X', and ice X, respectively. These transitions are not sharp; certainly not of first order (no volume collapse), unlikely of second order (no discontinuous changes in bulk modulus). This association suggests that the compressive behavior of H₂O at high pressure is sensitive to proton ordering. Our results further confirm computational predictions that the bulk modulus of ice X is distinctly higher than that of ice VII.

ACKNOWLEDGMENTS

This research was supported through the German Science Foundation (Deutsche Forschungsgemeinschaft, DFG) in Research Unit FOR 2440 (Grants No. MA4534/5-1 and No. STE1105/13-1). We acknowledge DESY (Hamburg, Germany), a member of the Helmholtz Association HG, for providing the experimental facility PETRA III and beamline P02.2. We acknowledge B. Winkler and the BMBF Project

No. 05K13RF1 for the purchase of the LAMBDA detectors and the laser cutting machine for preparing the gaskets. We thank Martin French for sharing water high-pressure results,

and Tiziana Boffa Balaran, Niccolò Satta, and Thomas Meier for helpful discussions. We also thank F. Lehmkuhler for his helpful review on this work.

- [1] J. J. Lissauer, D. C. Fabrycky, E. B. Ford, W. J. Borucki, F. Fressin, G. W. Marcy, J. A. Orosz, J. F. Rowe, G. Torres, W. F. Welsh, N. M. Batalha, S. T. Bryson, L. A. Buchhave, D. A. Caldwell, J. A. Carter, D. Charbonneau, J. L. Christiansen, W. D. Cochran, J.-M. Desert, E. W. Dunham, M. N. Fanelli, J. J. Fortney, T. N. Gautier, J. C. Geary, R. L. Gilliland, M. R. Haas, J. R. Hall, M. J. Holman, D. G. Koch, D. W. Latham, E. Lopez, S. McCauliff, N. Miller, R. C. Morehead, E. V. Quintana, D. Ragozzine, D. Sasselov, D. R. Short, and J. H. Steffen, *Nature (London)* **470**, 53 (2011).
- [2] R. Redmer, T. R. Mattsson, N. Nettelmann, and M. French, *Icarus* **211**, 798 (2011).
- [3] R. Jaumann, R. N. Clark, F. Nimmo, A. R. Hendrix, B. J. Buratti, T. Denk, J. M. Moore, P. M. Schenk, S. J. Ostro, and R. Srama, in *Saturn from Cassini-Huygens*, edited by M. K. Dougherty, L. W. Esposito, and S. M. Krimigis (Springer Netherlands, Dordrecht, 2009), pp. 637–681.
- [4] S. A. Kattenhorn and L. M. Prockter, *Nat. Geosci.* **7**, 762 (2014).
- [5] B. Journaux, I. Daniel, S. Petitgirard, H. Cardon, J.-P. Perrillat, R. Caracas, and M. Mezouar, *Earth Planet. Sci. Lett.* **463**, 36 (2017).
- [6] L. Noack, D. Höning, A. Rivoldini, C. Heistracher, N. Zimov, B. Journaux, H. Lammer, T. Van Hoolst, and J. H. Bredehöft, *Icarus* **277**, 215 (2016).
- [7] C. Sotin, O. Grasset, and A. Mocquet, *Icarus* **191**, 337 (2007).
- [8] A. D. Fortes and M. Choukroun, *Space. Sci. Rev.* **153**, 185 (2010).
- [9] J.-F. Lin, V. V. Struzhkin, S. D. Jacobsen, M. Y. Hu, P. Chow, J. Kung, H. Liu, H.-k. Mao, and R. J. Hemley, *Geophys. Res. Lett.* **32**, L11306 (2005).
- [10] B. Schwager and R. Boehler, *High Pressure Res.* **28**, 431 (2008).
- [11] O. Tschauner, S. Huang, E. Greenberg, V. B. Prakapenka, C. Ma, G. R. Rossman, A. H. Shen, D. Zhang, M. Newville, A. Lanzirotti, and K. Tait, *Science* **359**, 1136 (2018).
- [12] J. D. Bernal and R. H. Fowler, *J. Chem. Phys.* **1**, 515 (1933).
- [13] W. B. Holzapfel, *J. Chem. Phys.* **56**, 712 (1972).
- [14] M. Benoit, D. Marx, and M. Parrinello, *Nature (London)* **392**, 258 (1998).
- [15] M. Benoit, A. H. Romero, and D. Marx, *Phys. Rev. Lett.* **89**, 145501 (2002).
- [16] M. Benoit and D. Marx, *ChemPhysChem* **6**, 1738 (2005).
- [17] L. Lin, J. A. Morrone, and R. Car, *J. Stat. Phys.* **145**, 365 (2011).
- [18] E. Sugimura, T. Itaka, K. Hirose, K. Kawamura, N. Sata, and Y. Ohishi, *Phys. Rev. B* **77**, 214103 (2008).
- [19] E. Wolanin, Ph. Pruzan, J. C. Chervin, B. Canny, M. Gauthier, D. Häusermann, and M. Hanfland, *Phys. Rev. B* **56**, 5781 (1997).
- [20] M. Guthrie, R. Boehler, J. J. Molaison, B. Haberl, A. M. dos Santos, and C. Tulk, *Phys. Rev. B* **99**, 184112 (2019).
- [21] A. F. Goncharov, N. Goldman, L. E. Fried, J. C. Crowhurst, I.-Feng W. Kuo, C. J. Mundy, and J. M. Zaug, *Phys. Rev. Lett.* **94**, 125508 (2005).
- [22] K. Aoki, H. Yamawaki, M. Sakashita, and H. Fujihisa, *Phys. Rev. B* **54**, 15673 (1996).
- [23] A. F. Goncharov, V. V. Struzhkin, M. S. Somayazulu, R. J. Hemley, and H. K. Mao, *Science* **273**, 218 (1996).
- [24] M. Song, H. Yamawaki, H. Fujihisa, M. Sakashita, and K. Aoki, *Phys. Rev. B* **60**, 12644 (1999).
- [25] M. Song, H. Yamawaki, H. Fujihisa, M. Sakashita, and K. Aoki, *Phys. Rev. B* **68**, 014106 (2003).
- [26] C.-S. Zha, R. J. Hemley, S. A. Gramsch, H. Mao, and W. A. Bassett, *J. Chem. Phys.* **126**, 074506 (2007).
- [27] P. Loubeyre, R. LeToullec, E. Wolanin, M. Hanfland, and D. Häusermann, *Nature (London)* **397**, 503 (1999).
- [28] C.-S. Zha, J. S. Tse, and W. A. Bassett, *J. Chem. Phys.* **145**, 124315 (2016).
- [29] T. Meier, S. Petitgirard, S. Khandarkhaeva, and L. Dubrovinsky, *Nat. Commun.* **9**, 2766 (2018).
- [30] W. J. Evans, C.-S. Yoo, G. W. Lee, H. Cynn, M. J. Lipp, and K. Visbeck, *Rev. Sci. Instrum.* **78**, 073904 (2007).
- [31] Zs. Jenei, H.-P. Liermann, R. Husband, A. S. J. Méndez, D. Pennicard, H. Marquardt, E. F. O'Bannon, A. Pakhomova, Z. Konopkova, K. Glazyrin, M. Wendt, S. Wenz, E. E. McBride, W. Morgenroth, B. Winkler, A. Rothkirch, M. Hanfland, and W. J. Evans, *Rev. Sci. Instrum.* **90**, 065114 (2019).
- [32] H. Marquardt, J. Buchen, A. S. J. Méndez, A. Kurnosov, M. Wendt, A. Rothkirch, D. Pennicard, and H.-P. Liermann, *Geophys. Res. Lett.* **45**, 6862 (2018).
- [33] A. S. J. Méndez, H. Marquardt, R. J. Husband, I. Schwark, J. Mainberger, K. Glazyrin, A. Kurnosov, C. Otzen, N. Satta, J. Bednarcik, and H.-P. Liermann, *Rev. Sci. Instrum.* **91**, 073906 (2020).
- [34] H.-P. Liermann, Z. Konôpková, W. Morgenroth, K. Glazyrin, J. Bednarcik, E. E. McBride, S. Petitgirard, J. T. Delitz, M. Wendt, Y. Bican, A. Ehnes, I. Schwark, A. Rothkirch, M. Tischer, J. Heuer, H. Schulte-Schrepping, T. Krachta, and H. Franz, *J. Synchrotron Radiat.* **22**, 908 (2015).
- [35] D. Pennicard, S. Smoljanin, F. Pithan, M. Sarajlic, A. Rothkirch, Y. Yu, H. P. Liermann, W. Morgenroth, B. Winkler, and Z. Jenei, *J. Instrum.* **13**, C01026 (2018).
- [36] D. Pennicard, S. Lange, S. Smoljanin, H. Hirsemann, H. Graafsma, M. Epple, M. Zuvic, M.-O. Lampert, T. Fritzsche, and M. Rothermund, *J. Phys. Conf. Ser.* **425**, 062010 (2013).
- [37] C. Prescher and V. B. Prakapenka, *High Pressure Res.* **35**, 223 (2015).
- [38] S. P. Ong, W. D. Richards, A. Jain, G. Hautier, M. Kocher, S. Cholia, D. Gunter, V. L. Chevrier, K. A. Persson, and G. Ceder, *Comput. Mater. Sci.* **68**, 314 (2013).
- [39] M. Newville, R. Otten, A. Nelson, A. Ingargiola, T. Stensitzki, D. Allan, A. Fox, F. Carter, D. P. Michał, Y. Ram, C. D. Glenn, A. B. Stuermer, O. Frost, N. Zobrist, G. P. Mark, A. L. R. Hansen, T. Spillane, S. Caldwell, A. Polloreno, J. F. Andrewhanum,

- B. F. Maier, B. Gamari, A. Persaud, and A. Almarza (Zenodo, 2020), <https://zenodo.org/record/3814709#.YAvFOV4zaUl>.
- [40] Y. Fei, A. Ricolleau, M. Frank, K. Mibe, G. Shen, and V. Prakapenka, *Proc. Natl. Acad. Sci. U.S.A.* **104**, 9182 (2007).
- [41] See Supplemental Material at <http://link.aps.org/supplemental/10.1103/PhysRevB.103.064104> for further details of the data treatment and bulk modulus calculation as well as a comparison of the bulk moduli obtained in this work for dDAC-1, dDAC-2, and dDAC-3.
- [42] P. Dierckx, *J. Comput. Appl. Math.* **1**, 165 (1975).
- [43] P. Dierckx, *SIAM J. Numer. Anal.* **19**, 1286 (1982).
- [44] M. French and R. Redmer, *Phys. Rev. B* **91**, 014308 (2015).
- [45] S. Klotz, K. Komatsu, H. Kagi, K. Kunc, A. Sano-Furukawa, S. Machida, and T. Hattori, *Phys. Rev. B* **95**, 174111 (2017).
- [46] J. S. Zhang, M. Hao, Z. Ren, and B. Chen, *Appl. Phys. Lett.* **114**, 191903 (2019).
- [47] X. Li, W. Shi, X. Liu, and Z. Mao, *Am. Miner.* **104**, 1307 (2019).
- [48] M. Ahart, M. Somayazulu, S. A. Gramsch, R. Boehler, H. Mao, and R. J. Hemley, *J. Chem. Phys.* **134**, 124517 (2011).
- [49] Y. Asahara, K. Hirose, Y. Ohishi, N. Hirao, and M. Murakami, *Earth Planet. Sci. Lett.* **299**, 474 (2010).
- [50] M. Kuriakose, S. Raetz, Q. M. Hu, S. M. Nikitin, N. Chigarev, V. Tournat, A. Bulou, A. Lomonosov, P. Djemia, V. E. Gusev, and A. Zerr, *Phys. Rev. B* **96**, 134122 (2017).
- [51] B. Journaux, R. Caracas, P. Carrez, K. Gouriet, P. Cordier, and I. Daniel, *Phys. Earth Planet. Inter.* **236**, 10 (2014).
- [52] S. Speziale, H. Marquardt, and T. S. Duffy, *Rev. Mineral. Geochem.* **78**, 543 (2014).
- [53] A. F. Goncharov, V. V. Struzhkin, H. K. Mao, and R. J. Hemley, *Phys. Rev. Lett.* **83**, 1998 (1999).
- [54] V. V. Struzhkin, A. F. Goncharov, R. J. Hemley, and H. K. Mao, *Phys. Rev. Lett.* **78**, 4446 (1997).
- [55] F. Trybel, M. Cosacchi, T. Meier, V. M. Axt, and G. Steinle-Neumann, *Phys. Rev. B* **102**, 184310 (2020).